PHYSICAL SCIENCES

Programmed mechano-chemical coupling in reaction-diffusion active matter

Anis Senoussi*†, Jean-Christophe Galas*, André Estevez-Torres*

Embryo morphogenesis involves a complex combination of self-organization mechanisms that generate a great diversity of patterns. However, classical in vitro patterning experiments explore only one self-organization mechanism at a time, thus missing coupling effects. Here, we conjugate two major out-of-equilibrium patterning mechanisms—reaction-diffusion and active matter—by integrating dissipative DNA/enzyme reaction networks within an active gel composed of cytoskeletal motors and filaments. We show that the strength of the flow generated by the active gel controls the mechano-chemical coupling between the two subsystems. This property was used to engineer a synthetic material where contractions trigger chemical reaction networks both in time and space, thus mimicking key aspects of the polarization mechanism observed in *C. elegans* oocytes. We anticipate that reaction-diffusion active matter will promote the investigation of mechano-chemical transduction and the design of new materials with life-like properties.

INTRODUCTION

Living embryos get their shape through a complex combination of biochemical and mechanical mechanisms that process morphogenetic information according to two prototypical modes (*1*): a deterministic and a self-organized one. In the deterministic mode, genes determine biochemical reactions that influence mechanical deformations of cells and tissues following a hard-wired program. In the self-organized mode, biochemical reactions and mechanical processes generate large-scale spatiotemporal order from an initial homogeneous situation. Order thus arises through chemical and mechanical instabilities that amplify random fluctuations into patterns with well-defined length and time scales (*2*). Two key points characterize the self-organization mode: It is an intrinsically nonequilibrium process that continuously dissipates energy, and couplings occur in both directions between the biochemical and the mechanical subsystems (*1*). Self-organization arises, for instance, during the early development of *C. elegans*, where local contractions of the actomyosin cortex induce cytoplasmic flows that trigger a reaction-diffusion instability in the PAR reaction network, inducing embryo polarization (*3*).

Both the deterministic and the self-organization mechanisms are useful conceptual frameworks to produce life-like synthetic materials and to investigate morphogenetic models in a controlled environment for testing theoretical predictions (*4*, *5*). Inspired by the self-organization mode, here, we explore in vitro the coupling of two independent self-organizing molecular subsystems, a mechanical and a chemical one. The investigation of self-organization in vitro has been a subject of intense scrutiny for several decades. Chemical self-organization arises from reaction networks driven out of equilibrium by the consumption of a chemical fuel. It produces spatiotemporal concentration patterns through reaction or reaction-diffusion instabilities that have been observed in vitro from a reduced set of chemistries (*6*–*13*). Mechanical self-organizationemerges in active matter, which converts chemical energy into mechanical work, generating fluid flows through hydrodynamic instabilities (*14*). Molecular active matter is generally made of cytoskeletal motors and filaments reconstituted in vitro (*4*). So called active gels produce a variety of static patterns (*15*), flows (*16*–*20*), or both (*21*–*24*).

In addition to studying chemical and mechanical self-organization independently, efforts have also focused on coupling chemistry and mechanics in self-organized systems. Classical experiments used redox oscillators such as the Belousov-Zhabotinsky reaction to drive the mechanical perturbation of a hydrogel and create self-oscillating gels (*25*, *26*). There, chemical self-organization was translated into changes in the mechanical properties of a material but the latter was unable of mechanical self-organization by itself. Other important works report DNA reactions that control the mechanical properties of either passive (*27*) or active gels (*28*–*30*). However, in these examples, only one of the two systems could be maintained out of equilibrium, either the reaction network (*25*), or the gel (*27*–*31*), and thus only one of them could exhibit spatiotemporal self-organization. A notable example created a chemo-mechano-chemical oscillator, a class of temporal self-organization, by combining chemical and mechanical feedbacks (*32*). In this case, self-organization emerged through the coupling of two subsystems that were unable to self-organize when considered independently. In contrast, embryo development establishes couplings between chemical and mechanical subsystems that are, each of them, independently capable of self-organization (*1*, *33*, *34*). It is thus important to design self-shaping materials that couple two self-organizing subsystems, as recently shown by Gavriljuk *et al.* (*35*).

RESULTS

To create a functional mechano-chemical dissipative material, we assembled two dissipative molecular subsystems, a chemical and a mechanical one. The chemical subsystem is made of a network of DNA/enzyme reactions that produce single-stranded DNA (ssDNA) molecules (Fig. 1A) (*12*). The mechanical subsystem is an active gel composed of bundles of protein filaments propulsed by molecular motors (Fig. 1B) (*15*, *17*). Each subsystem is maintained out of equilibrium via the hydrolysis of high-energy compounds, respectively, deoxynucleoside triphosphates and adenosine triphosphate (ATP).

Sorbonne Université, CNRS, Institut de Biologie Paris-Seine (IBPS), Laboratoire Jean Perrin (LJP), F-75005 Paris, France.
*Corresponding author. Email: anis.senoussi@espci.psl.eu (A.S.); jean-christophe.galas@sorbonne-universite.fr (J.-C.G.); andre.estevez-torres@sorbonne-universite.fr (A.E.-T.)
†Laboratoire Gulliver, CNRS, ESPCI Paris, PSL Research University, 10 Rue Vauquelin 75005 Paris, France.

The chosen chemical subsystem has four advantages. First, because of DNA hybridization rules, it can be easily reprogrammed into a variety of dissipative dynamics such as oscillations (*36*), bistability, and excitability (*37*). Second, it can be maintained out of equilibrium in a closed reactor for days (*38*). Third, working in water at pH 7, it is a priori compatible with other biochemical reactions (*39*). Last, it generates a variety of reaction-diffusion patterns such as traveling fronts (*40*), waves (*13*), and stationary patterns (*41*). In a first series of experiments, the chemical subsystem encoded an autocatalytic loop that produces ssDNA species **A**, the node, in the presence of ssDNA $\mathbf{T}_{AA}$, the template, a polymerase and a nicking enzyme (Fig. 1A) (*12*).

In the mechanical subsystem, the bundles are constituted of stabilized microtubule filaments assembled together by attracting forces generated by the presence of a depletion agent (Fig. 1B) (*17*). The motors are clusters of kinesin-1 and thus can bind several microtubules at once (see Materials and Methods). Such an active gel generates macroscopic flows that, depending on the concentration of motors and filaments, produce a diversity of microtubule morphologies (*4*, *5*): local contractions (*15*), corrugations (*24*), chaotic flows (*17*), and global contractions (*21*). In the following, we demonstrate that, when mixed together, the two subsystems retain their ability to undergo, respectively, chemical and mechanical instabilities that generate spatiotemporal patterns. We further show that the strength of the active flow generated by the mechanical subsystem controls the mechanochemical coupling between the two subsystems (Fig. 1D). Last, we take advantage of this property to design materials that mimic the mechano-chemical transduction mechanism defining the polarity of the *C. elegans* embryo (Fig. 1E) (*3*).

To check whether the two subsystems remained functional when combined in an optimized buffer (fig. S1), we tested the propagation of a DNA front through and active gel undergoing local contractions. To do so, a solution containing all the components of the chemical and mechanical subsystems, except the strand **A**, were filled into a microchannel.

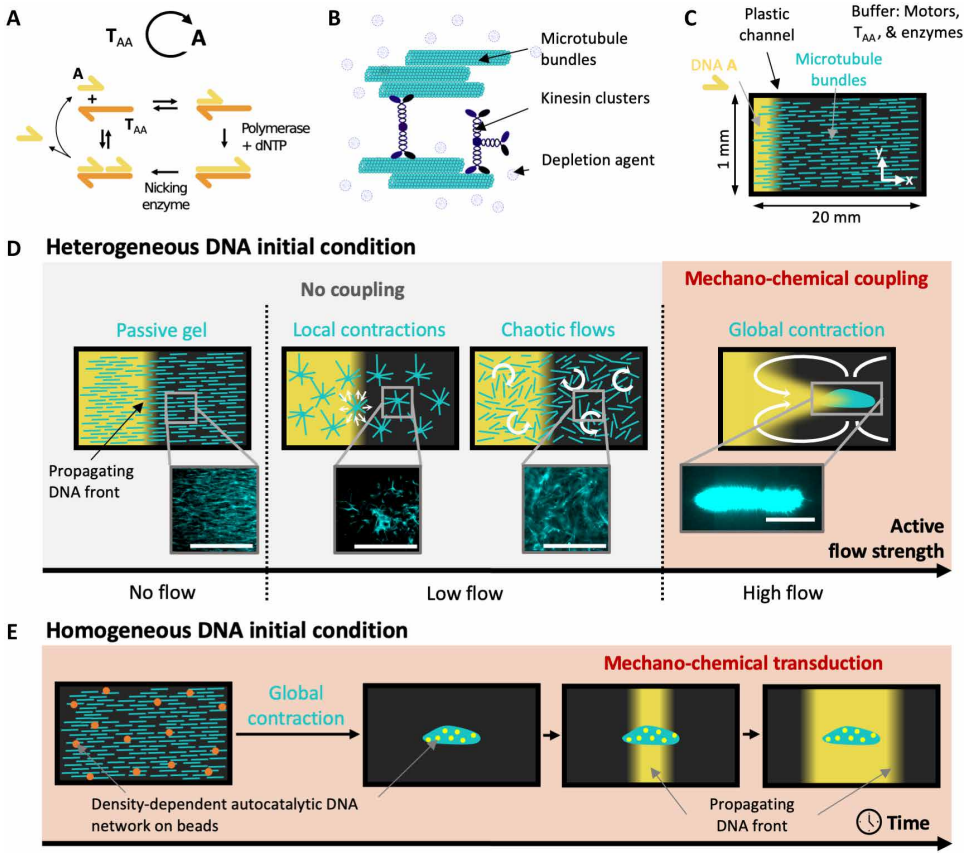

Fig. 1. In a reaction-diffusion active matter system, the mechano-chemical coupling is controlled by the strength of the active flow and it can be used to engineer mechano-chemical transduction in a synthetic material. (**A**) Scheme of the chemical subsystem involving the autocatalytic amplification of DNA strand A in the presence of enzymes and template strand $\mathbf{T}_{AA}$. Harpoon-ended arrows denote ssDNA. (**B**) Cartoon of the mechanical subsystem: an active gel formed by microtubules bundled together by a depletion agent and clusters of kinesin-1 motors. (**C**) Sketch of the channel in which the DNA front propagation and the active gel dynamics were observed by fluorescence microscopy. In most experiments, A (yellow) is initially present only on the left side and the microtubule bundles (light blue) are aligned along *x*. (**D**) A mechano-chemical coupling between the two subsystems is achieved by increasing the strength of the flows generated by the active gel, which induces four different microtubule structures (light blue) and two DNA patterns (yellow). The white arrows represent the hydrodynamic flows generated by the active gel. Fluorescence images of the microtubules are represented for each morphology. Scale bars, 0.5 mm. (**E**) When the initial condition of DNA A is homogeneously distributed and the kinetics of DNA autocatalysis depend on the density of the active gel, gel contraction is transduced into a DNA propagating front starting at the position of the contracted gel.

An initial condition containing the same solution supplemented with **A** was injected on the left side of the channel (Fig. 1C). We recorded the spatiotemporal dynamics of each subsystem by fluorescence microscopy thanks to the presence of a DNA intercalator that becomes fluorescent upon binding to double-stranded DNA (dsDNA) and of fluorescently labeled microtubules (see Materials and Methods). In the chemical subsystem, we observed the propagation of a front of DNA fluorescence with constant velocity v_c = 20 μm/min across the whole length of the active gel, i.e., >1 cm (Figs. 1D and 2A, fig. S2, and movie S1). Concomitantly, in the mechanical subsystem the microtubules contracted locally with a characteristic time τ_m = 50 min into aggregates with a typical size of 100 to 500 μm. The observation of a DNA front and microtubule aggregates is in agreement with previous reports for each subsystem taken independently (*15*, *40*).

When the active gel produces local contractions, the dynamics of each subsystem can be independently tuned. Increasing the polymerase concentration, [pol], increases the front velocity, v_c, until reaching a plateau at 22 μm/min (Fig. 2B). In these conditions, the characteristic contraction time τ_m remained constant. We find a scaling $v_c \sim [\text{pol}]^{1/2}$, in agreement with previous results (*40*) and characteristic of Luther reaction-diffusion dynamics where $v_c \sim r_c^{1/2}$, taking $r_c \sim [\text{pol}]$ for the rate of the autocatalytic reaction as observed in previous experiments (*40*). In turn, when the motor concentration, [motor], increases, τ_m decreases until reaching a plateau at 100 min (Fig. 2C) and the size of microtubule aggregates increases (fig. S3), while v_c remains constant. A hydrodynamic model of a contracting active gel (*5*) yields $\tau_m^{-1} \sim \zeta([\text{motor}])$, where ζ is the strength of the gel activity, which depends on the motor concentration, and two scalings are found in the literature (*18*, *42*) yielding $\tau_m \sim [\text{motor}]^{-\alpha}$, with α = 1 or 2 (Supplementary Text). Our data are compatible with both scalings (Fig. 2C). In summary, Fig. 2 shows that the two subsystems are both chemically and mechanically decoupled when the gel undergoes local contractions.

By varying the conditions, we can propagate the chemical front through active gels undergoing other spatial instabilities associated with different active flow strengths, as sketched in Fig. 1D. When the 2′-deoxyguanosine 5′-triphosphate (dGTP) concentration was reduced (figs. S4 and S5), chaotic flows were observed in the mechanical subsystem during several hours before local contractions occurred (movie S2). Such flows did not modify the velocity of the chemical front because transport remained dominated by Brownian diffusion. The velocity of the flow was estimated to be v_m = 8 μm/min, which, considering the typical size of a fluid vortex, $l_m \approx 125$ μm, and the diffusion coefficient of DNA **A**, $D_A = 12 \times 10^3$ μm^2/min, yields a Péclet number $\text{Pe} = v_m l_m / D_A \approx 0.08$ (Supplementary Text). Note, however, that kinesin/microtubule active gels may reach flows up to 600 μm/min (*43*), which would result in Pe ≈ 5 and thus in a substantial perturbation of the front by the flow. Such large flows were not observed here. When microtubules were stabilized using taxol, which increases their average length, and the motor concentration reduced, the active gel formed corrugations reminiscent of those previously reported in the absence of the chemical subsystem (*24*), again without perturbing the chemical front (movie S3).

In contrast, a marked perturbation of the front propagation was observed when the active gel underwent a global contraction, associated with large hydrodynamic flows characterized by a high Péclet number (Fig. 3, figs. S6 to S11, and movie S4). Global contractions were observed for long microtubules and relatively high motor concentrations (fig. S7). When the gel contracted more rapidly than the front propagated, the front moved faster and we distinguished four phases (Fig. 3C). During phase I, the active gel contracted rapidly toward the center of the channel, accelerating until reaching a maximum velocity v_m = 400 μm/min at the end of phase I and dragging DNA along, which formed a detached DNA islet ahead of the front. During phase II the gel decelerated and the DNA islet was diluted in the *xy* plane resulting in a front with a skewed profile fivefold wider than the initial one (fig. S6). Throughout phases I and II, the Péclet number was greater than 1 (fig. S8), indicating that active convection predominated over diffusion. Last, when the active gel stopped contracting, the DNA front slowly recovered a sigmoidal shape (phase III; fig. S6) and eventually reached a steady state with constant velocity and width (phase IV).

In a control experiment with a passive dye, only phases I and II were observed, indicating that reaction was necessary for phases III

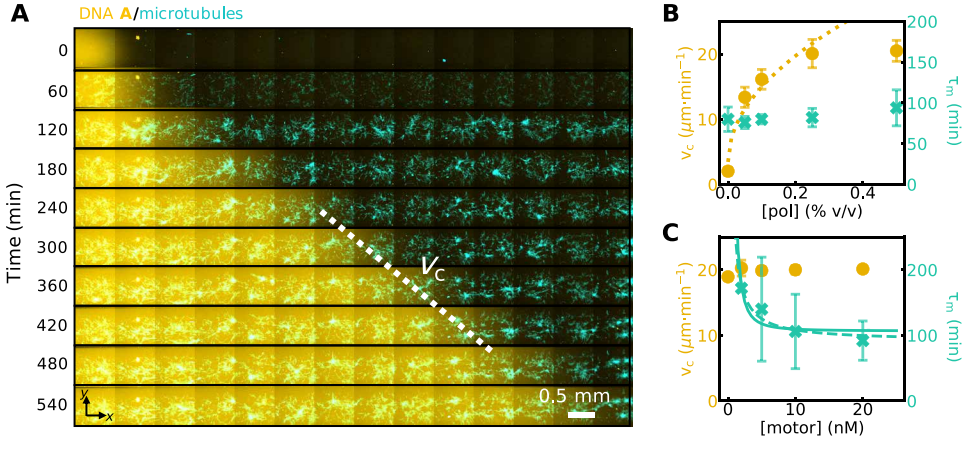

Fig. 2. A DNA/enzyme reaction-diffusion front propagates at constant velocity inside a locally contracting cytoskeletal active gel and the dynamics of each subsystem can be independently tuned. (**A**) Time-lapse two-color image of the fluorescence intensities associated to species A (yellow) and to the microtubule network (light blue) (see also movie S1). The dotted line indicates the velocity of the chemical front, $\boldsymbol{v_c}$. (**B** and **C**) Plots of $\boldsymbol{v_c}$ (yellow disks) and contraction time of the active gel, $\boldsymbol{\tau_m}$, (blue crosses) for different concentrations of DNA polymerase (B) and motors (C). The lines are fits to the data with $\boldsymbol{v_c} \sim [\textbf{pol}]^{1/2}$ (dotted line), $\boldsymbol{\tau_m} \sim [\textbf{motor}]^{-1}$ (dashed line), and $\boldsymbol{\tau_m} \sim [\textbf{motor}]^{-2}$ (plain line). Error bars correspond to one SD from a triplicate experiment.

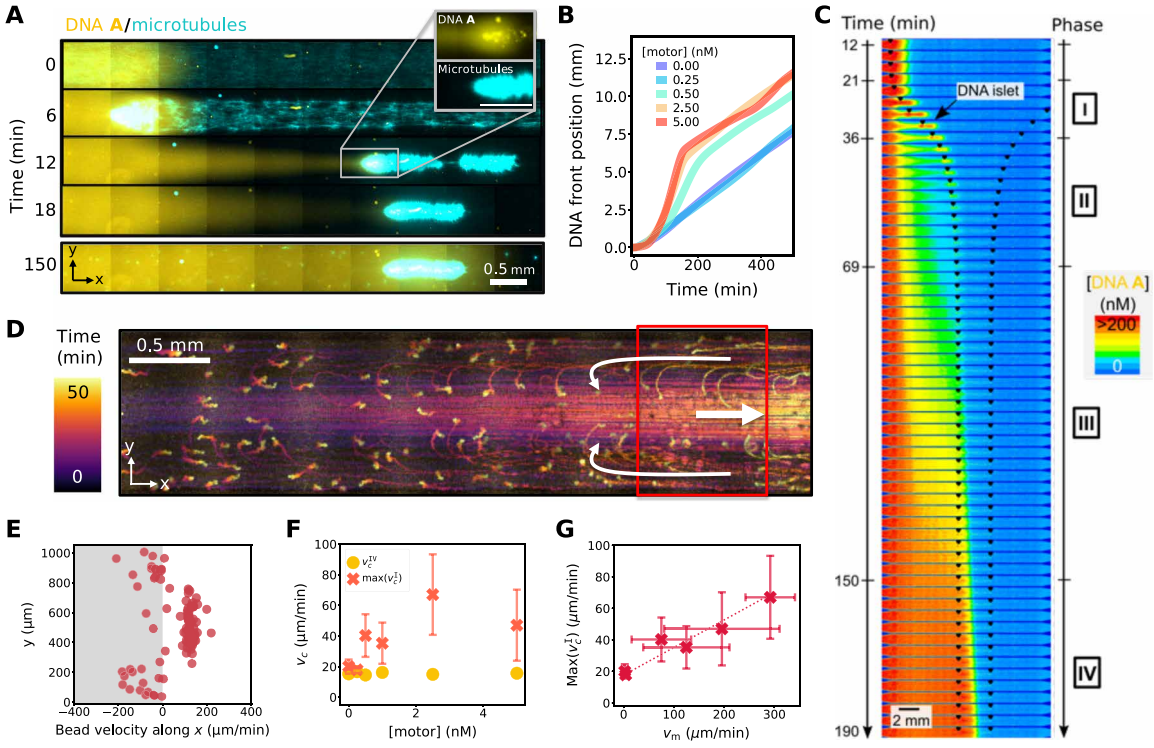

Fig. 3. A globally contracting active gel stretches and accelerates a reaction-diffusion front. (**A**) Time-lapse, two-color fluorescence image with the DNA front in yellow and the microtubules in light blue. The inset shows the two fluorescence channels in separate images for the selected region. The white and yellow spots are dust particles concentrated by the contracting gel (see also movie S4). (**B**) Position of the DNA front along *x* for different motor concentrations. (**C**) Time-lapse images of DNA fluorescence (color) at [motor] = 2.5 nM and 3 min per image. The extremities of the contracting gel are indicated with black markers. Roman numbers indicate the four phases described in the text. (**D**) Stroboscopic image averaged over 50 min showing the trajectories of fluorescent beads during gel contraction, and the white arrows indicate the sense of the flow (see also movie S5) and (**E**) plot of the bead velocity along *x* across the width of the channel for the beads in the red rectangle, 25 min after the beginning of the contraction. (**F**) Maximal front velocity during phase I (crosses) and steady-state velocity during phase IV (disks) for different motor concentrations. (**G**) Maximal front velocity during phase I versus maximal gel contraction velocity. Error bars correspond to one SD from a triplicate experiment.

and IV and that DNA islet formation was not related to the binding of DNA to the active gel (fig. S10). We confirmed the last interpretation by adding passive brownian beads to measure the hydrodynamic flow induced during contraction. We observed two counter-rotating fluid rolls, symmetric along the central axis of the channel, *x*, and producing water flows along *x* that reached +150 μm/min in the center of the channel and −100 μm/min at its borders (Fig. 3, D and E; fig. S11; and movie S5). We thus conclude that the stretching of the concentration profile of **A** leading to the formation of the DNA islet during phase I was a purely hydrodynamic process.

The active gel contraction velocity, v_m, was a sigmoidal function of the motor concentration (fig. S7). We quantified the two main regimes of front propagation with max (v_c^I) the maximal velocity during phase I and v_c^{IV} the velocity at steady state in phase IV. Figure 3F shows that the former strongly depended on the motor concentration while the latter was independent. Last, the linear relationship between max (v_c^I) and v_m is consistent with the observation of a convection-dominated transport during phase I (Fig. 3G). Together, these results show that when the flows generated by the active gel are sufficiently fast there is a mechano-chemical coupling between the gel and the reaction-diffusion front. This coupling happens through hydrodynamics and can be interpreted as a time-dependent Taylor dispersion (*44*).

We have just seen that active flows can substantially modify heterogeneous concentration profiles present in the chemical subsystem. In the following, we will show that homogeneous concentration profiles can also be mechanically modulated and we will engineer a mechano-chemical transduction pathway in this context. This is precisely what happens in the *C. elegans* embryo, where the active flow generated by the actomyosin cortex breaks the symmetry of an initially homogeneous distribution of PAR proteins. Later, this asymmetry is amplified by a PAR-dependent bistable reaction network, leading to embryo polarization (*3*). The reaction-diffusion active matter system developed here is a good candidate to mimic this process in a synthetic material. To do so, we first need to implement a mechanism that couples a variation in the microtubule concentration with a change in the concentration of a DNA species that is initially homogeneously distributed. Second, we need to engineer a chemical network that amplifies this concentration change.

The first requirement was fulfilled by attaching DNA strands to ~30-μm-diameter hydrogel beads, which were trapped by the microtubule mesh and concentrated during contraction. The second condition was satisfied by engineering a chemical subsystem whose kinetics depend on the concentration of DNA bead conjugates and thus on the contraction state of the gel. More precisely, the DNA autocatalytic loop was split into two nodes, **B** and **D**, that cross-activate each other thanks to the templates $\mathbf{T}_{BD}$ and $\mathbf{T}_{DB}$ (Fig. 4A). By attaching each of these biotin-modified templates to a set of

streptavidin-coated hydrogel beads and supplementing the medium with an exonuclease that degrades **B** and **D** (Fig. 4A) the cross-catalysis kinetics become diffusion controlled (*45*) and thus should depend on bead density. As a result, the beads brought together in a contracted gel should activate faster, producing dsDNA that lights them up in the presence of a DNA intercalator dye (Fig. 4B). When both types of beads where embeddedin the active gel in the presence of a homogeneous, low concentration of **D**, they first reached a high density as the gel contracted and later they became fluorescent (Fig. 4, C and D, and movie S6), starting from the locations where the two types of beads were closer to each other (fig. S13). In the absence of contraction, the bead fluorescence amplification was delayed (fig. S12) and its final amplitude reduced, both by a factor 2 (Fig. 4D). As expected for diffusion-controlled kinetics, the mechano-chemical DNA amplification dynamics slowed down with increasing exonuclease concentration (Fig. 4D). Triplicate experiments revealed the robustness of this mechano-chemical transduction process.

To show that the activated beads may trigger downstream reactions in solution, we sought to use the contraction-driven cross-autocatalytic network just described to trigger a propagating DNA front. To do so, the cross-autocatalytic system of Fig. 4 (A and B) was supplemented with freely diffusing templates $\mathbf{T}_{BA}$ and $\mathbf{T}_{AA}$, which respectively convert **B** into **A** and sustain the front-producing, autocatalytic reaction of **A** outlined in Fig. 1A. In addition, to suppress the undesired self-activation of $\mathbf{T}_{AA}$, a repressor strand $\mathbf{R}_A$ was added (Fig. 5A)

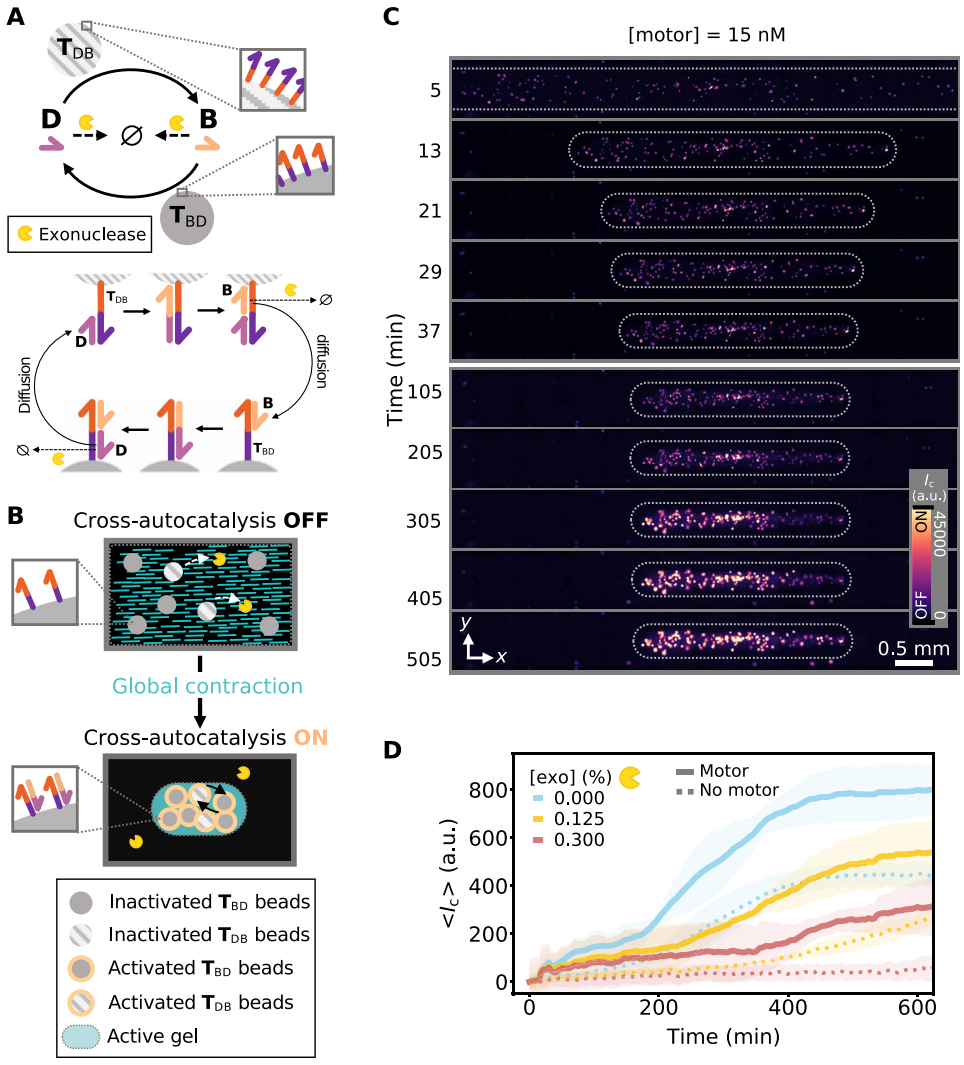

Fig. 4. A globally contracting active gel triggers a downstream reaction network with temporal control. (**A**) Scheme of the cross-autocatalytic DNA/enzyme network (top). Plain and dotted arrows indicate activation and degradation reactions, respectively. Harpoon-ended arrows correspond to ssDNA and disks indicate hydrogel beads carrying templates T_{ij}. Detailed mechanism of bead activation where the diffusion of B and D between beads is indicated (bottom). (**B**) Sketch of the mechano-chemical activation of the reaction network in (A) through the contraction of the active gel (light blue) that brings the hydrogel beads (disks) close together, speeding up cross-catalysis. The beads become bright upon the formation of dsDNA. (**C**) Time-lapse images of DNA fluorescence from the template-bearing beads embedded in the active gel in the presence of motors. White dotted lines indicate the borders of the active gel and the channel walls are depicted in gray. a.u., arbitrary units. (**D**) Average DNA fluorescence over the whole channel versus time in the absence (dotted line) and in the presence (plain line) of motors for different exonuclease concentrations (colors). Shading around the lines corresponds to one standard deviation of three independent experiments.

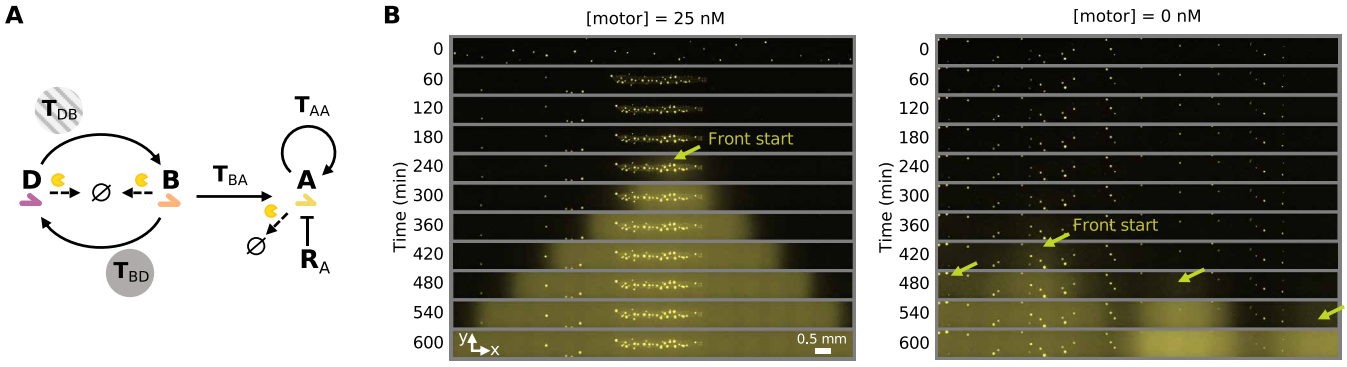

Fig. 5. The beads activated by the global contraction of the active gel trigger an autocatalytic front with spatial control. (**A**) Scheme of the bead-associated cross-autocatalytic network coupled to the autocatalysis of A in solution. Disks indicate templates linked to hydrogel beads. The blunt-ended arrow indicates repression. (**B**) Time-lapse images of DNA fluorescence in the channel for the network in (A), in the presence (left) and in the absence (right) of motors. The bright spots are the beads, the arrows indicate the start of the fronts of A, in yellow.

(*37*). In the presence of motors, the beads were all activated within 2 hours at the center of the channel, where the gel contracted, and they triggered a controlled front of **A** that propagated from the center of the channel to its extremities (Fig. 5B and movie S7). In contrast, in the absence of gel contraction, the beads randomly activated over the course of 5 hours, which was followed by the uncontrolled amplification of **A**. Increasing the concentration of one type of beads ($\mathbf{T}_{DB}$), while keeping the concentration of the other type constant ($\mathbf{T}_{BD}$), resulted in multiple uncontrolled fronts in the absence of kinesin motors (fig. S14). By doing, so we decrease the average distance between the two bead types and thus increase the probability of effective autocatalysis. We found that the presence of the repressor strand $\mathbf{R}_A$ was essential to prevent front activation at random positions. However, when the concentration of the repressor was greater than 500 nM, the front propagation was inhibited (fig. S15).

Together, these results demonstrate that a mechano-chemical transduction pathway can be engineered between a mechanical and a chemical self-organizing molecular system. In particular, they show that a mechanical instability may trigger either a temporal or a spatiotemporal chemical instability in a synthetic material.

DISCUSSION

The coupling of chemical and mechanical self-organization is a key ingredient of biological complexity, in particular, during embryogenesis (*1*, *34*). We have demonstrated that it is possible to couple two archetypal self-organization mechanisms, reaction-diffusion and active matter, in a synthetic material. Our design is modular because it relies on two distinct subsystems with well-characterized and predictable spatiotemporal behaviors: DNA/enzyme reactions and kinesin/microtubule active gels. Considered independently, each subsystem displays complex dynamics and macroscopic organizations that are subject to intense scrutiny (*13*, *15*, *17*, *19*, *21*, *24*, *39*, *41*).

We have shown that, when mixed together, the strength of the mechano-chemical coupling between the two subsystems is set by the magnitude of the flow generated by the active gel. This coupling was shown for a single pair of mechanical and chemical instabilities (global contraction and autocatalysis). However, the outcome of the coupling between other existing instabilities remains to be explored: oscillations (*36*), waves (*13*), band patterns (*41*)—for the chemical subsystem—and chaotic flows (*19*), local contractions, and active foams (*46*)—for the mechanical subsystem. For instance, the behavior of the enumerated reaction-diffusion states within chaotic flows with high Péclet number is currently unknown. In this exploration, the tunability of the two subsystems will be a major asset. The chemical subsystem is programmable because the reaction network is encoded in the sequence of DNA strands (*47*), while the mechanical subsystem can be heuristically designed thanks to the diversity of motors and filament-binding proteins available (*48*). In addition, the implementation of the reverse chemo-mechanical coupling, from chemistry to mechanics, recently described (*49*) and complementary to the one discussed here, would allow the investigation of self-organization in bidirectionally coupled subsystems. The future investigation of the coupling between two different self-organizing systems will help in the understanding of how macro-scale patterns and structures emerge from microscopic components in nonequilibrium systems (*4*). In particular, it will allow to develop and test currently lacking theories to understand this link.

Last, reaction-diffusion active matter provides a framework for the rational engineering of functional out-of-equilibrium materials with life-like properties (*5*, *41*, *50*). It could be advantageously combined with the wide array of methods in DNA nanotechnology, such as nanostructure design (*51*), logic gates (*10*), analyte detection (*52*), or hydrogel swelling (*27*).

MATERIALS AND METHODS

Kinesin purification

Two different kinesins were used: K430 and K401. K430 is a truncated kinesin-1 (amino acid residues 1 to 430) from *Rattus norvegicus* designed by Furuta *et al.* (*53*). It bears a soluble SNAP-tag and forms clusters spontaneously (*24*). K401 is a truncated kinesin-1 from *Drosophila melanogaster* designed by Subramanian and Gelles (*54*), bearing a biotin function. It forms clusters in the presence of streptavidin (*15*). Kinesins were purified as previously described (*24*) (more details in the Supplementary Materials).

Microtubule polymerization

Tubulin and tetramethyl rhodamine isothiocyanate (TRITC)–labeled tubulin were purchased from Cytoskeleton Inc., dissolved at 10 mg/ml in 1× PEM-KOH buffer [80 mM PIPES (pH 6.8; adjusted with KOH), 1 mM EGTA, and 1 mM $MgCl_2$], flash-frozen, and stored at −80°C.

Taxol-stabilized microtubules were prepared in a polymerization mix consisting in 1× PEM-KOH, 1 mM GTP, 10% (w/v) glycerol, and tubulin at 5 mg/ml (including 2.5% of TRITC-labeled fluorescent tubulin). The mix was incubated at 37°C for 15 min. 20 μM of paclitaxel (referred in the main text and in the following as taxol) was added to the mix and let at 37°C for five more minutes. After polymerization, newly formed microtubules were centrifuged at room temperature for 10 min at 12,000*g* to remove free tubulin monomers. The microtubules were redissolved into 1× PEM-KOH, 1 mM GTP, 10% glycerol, 20 μM taxol, and kept in the dark at room temperature for few days.

Guanosine-5′-[(α,β)-methyleno]triphosphate (GMPCPP) (purchased from Jena Bioscience) was also used to form microtubules. They were polymerized in the presence of 1× PEM-KOH, 0.6 mM GMPCPP, 0.2 mM dithiothreitol (DTT), 10% (w/v) glycerol and tubulin at 5 mg/ml (including 2.5% fluorescent tubulin) at 37°C for 30 min and left at room temperature for 5 hours. They were used within the same day or flash-frozen and stored at −80°C.

Hydrogel beads functionalization

DNA-coated sepharose beads were prepared as previously described (*45*). Streptavidin sepharose beads (34 μm median diameter) were purchased from GE Healthcare and were supplied in a 20% ethanol solution. The concentration of the stock solution was 16,000 beads/μl. We prepared 100 μl of solution containing 2500 beads/μl functionalized with 0.2 nmol of biotin-DNA for these 10^5 beads at room temperature for 20 min in the Buffer B with a gentle agitation. Buffer B is composed of 0.6× PEM-KOH, 0.2× PEM-NaOH (for 1×: 80 mM PIPES, 1 mM EGTA, and 1 mM $MgCl_2$ adjusted with 135 mM NaOH to pH 7.1), 8.0 mM $MgSO_4$, and 1.5% (w/v) Pluronic F127. The beads were then subjected to three cycles of centrifugation (10,000*g*, 30 s), removal of supernatant, and wash with buffer B. DNA-coated sepharose beads were lastly conserved for few weeks at 4°C.

Preparation of solutions

The experimental conditions for each figure are provided in tables S2 to S5. Solutions were prepared from the buffer AM and the components listed in tables S2 to S5. Buffer AM is composed of 0.6× PEM-KOH (for 1×: 80 mM PIPES, 1 mM EGTA, and 1 mM $MgCl_2$ adjusted with 130 mM KOH to pH 6.9), 0.2× PEM-NaOH (for 1×: 80 mM PIPES, 1 mM EGTA, and 1 mM $MgCl_2$ adjusted with 135 mM NaOH to pH 7.1), 8.0 mM $MgSO_4$, 1.5% (w/v) Pluronic F127, 1.0 mM ATP, 10 mM creatine phosphate, creatine kinase (5.0 μg/ml), 3.0 mM DTT, 20 mM D-glucose, 1.0 mM Trolox, bovine serum albumin (0.5 mg/ml), and 0.5× SYBR Green I. Glucose oxidase and catalase were not included in experiments involving DNA attached on hydrogel beads because we found that it caused variation in their fluorescence intensity.

The three enzymes needed for the chemical subsystem were: the Bst DNA polymerase Large Fragment (New England BioLabs)—abbreviated as Bst LF or pol—and the nicking enzyme Nt.BstNBI (New England BioLabs)—abbreviated as NBI. The exonuclease ttRecJ was produced in-house as previously described (*55*). The DNA sequences used in this work are listed in table S1 and were purchased from Biomers.

Experiments were performed within 18 mm by 1 mm by 0.2 mm poly(methyl methacrylate) (PMMA) channels (Fluidic 152, ChipShop). For front propagation experiments, they were filled with 4.5 μl of the solution containing all the elements except the DNA **A**. The initial condition, containing the same solution with 1 μM of the DNA **A**, was injected on one side of the channel (0.25 μl). The surplus of liquid was carefully absorbed using a clean tissue. Last, both ends of the channel were closed using vacuum grease, starting from the side without the DNA **A** to avoid contamination and the appearance of a second front that would propagate in opposite direction to the main front.

Imaging

Epifluorescence images were obtained with a Zeiss Observer 7 automated microscope equipped with a Hamamatsu C9100-02 camera, a 10× or a 4× objective, a motorized stage, and controlled with MicroManager 1.4. Images were recorded automatically every 3 s to 8 min (depending on the experiment) using an excitation at 470 nm (observation of the DNA intercalator) and/or 550 nm (observation of the microtubules) with a CoolLED pE2 or a CoolLED pE-4000. The temperature was controlled thanks to a transparent TokaiHitThermoPlate. For optimal thermal conduction, mineral oil was added between the PMMA channels and the thermoplate on the microscope. The setup was put in place at least 30 min before the filling of the channels in order to be sure that the temperature equilibrium (25°C or 28°C) was reached.

Autocatalytic network T_{AA} dynamics in well-mixed tubes

Optimization experiments presented in fig. S1 were performed in well-mixed 200-μl tubes in a BioRad CFX qPCR machine using 10 μl of solution at the temperature of 25°C. Total DNA concentration was measured, thanks to the intercalating molecule SYBR Green I (Thermo Fisher Scientific) or Evagreen (Biotium).

Data processing

Time-lapse images from microscopy experiments were processed by ImageJ/Fiji (National Institutes of Health) and Python. Images of the channels were first cropped and rotated manually to compute the velocity of the chemical front v_c and the time related to the dynamics of the active gel τ_m.

Determination of v_c

The DNA front images were recorded using a 470-nm excitation. Using a Python routine, images were filtered using a gaussian filter. The intensity was normalized between 0 and 1. Last, the contrast was adjusted by putting 10% of the highest (respectively, lowest) intensity values to 1 (respectively, 0). At each time the intensity was averaged along the width of the channel (y axis). We fitted this one-dimensional array of averaged intensity by the expression $I_c = \frac{e^{(x_c-x)/l_0}}{1+e^{(x_c-x)/l_0}}$ where x_c is the position of the front (the intensity is equal to 0.5) and l_0 its width. Thus, we obtained the position of the front as a function of time. We computed the velocity of the front by fitting this function by an affine fit. For the experiments presented in Fig. 3, the velocity $\max(v_c^I)$ was obtained by first deriving the position and then by taking the first five maximum velocities. v_c^{IV} was computed using a linear fit after the transient regime.

Determination of τ_m

Fluorescent microtubules were recorded using a 550-nm excitation. To quantify the dynamics of active structures, we first applied a gaussian filter, normalized the intensity, and then computed the SD of the normalized intensity along the y axis (width) for each position x of the channel length and for each time point. The SD was then normalized and we computed τ_m as the time needed to reach 0.5 of this normalized SD.

Determination of v_m

Active gel dynamics was obtained by manually tracking small aggregates and/or dust embedded in the active gel. We chose the aggregates to be close to the border on the left (where the DNA front was initiated). The velocities were computed as the time derivative of the position. Max (v_m) was obtained by taking the average of the five maximal velocities.

Tracking of beads

In the experiments of Fig. 3 (D and E) 1-μm-diameter fluorescent beads (Estapor Fluorescent Functionalized Microspheres F1-XC 100, Merck) were added to the solution to study the velocity of the active gel and the surrounding fluid. The beads were used at the concentration of 0.0015% (v/v). The tracking of the beads was performed using the ImageJ plugin TrackMate (*56*) that calculated trajectories, which were then analyzed by a Python routine to compute the velocities (derivative of the positions).

SUPPLEMENTARY MATERIALS

Supplementary material for this article is available at https://science.org/doi/10.1126/sciadv.abi9865

REFERENCES AND NOTES

1. C. Collinet, T. Lecuit, Programmed and self-organized flow of information during morphogenesis. *Nat. Rev. Mol. Cell Biol.* **22**, 245–265 (2021).
2. M. C. Cross, P. C. Hohenberg, Pattern formation outside of equilibrium. *Rev. Mod. Phys.* **65**, 851–1112 (1993).
3. N. W. Goehring, P. K. Trong, J. S. Bois, D. Chowdhury, E. M. Nicola, A. A. Hyman, S. W. Grill, Polarization of PAR proteins by advective triggering of a pattern-forming system. *Science* **334**, 1137–1141 (2011).
4. D. Needleman, Z. Dogic, Active matter at the interface between materials science and cell biology. *Nat. Rev. Mater.* **2**, 17048 (2017).
5. A. Senoussi, Y. Vyborna, H. Berthoumieux, J.-C. Galas, A. Estevez-Torres, *Out-of-Equilibrium (Supra)molecular Systems and Materials* (John Wiley & Sons, Ltd, 2021), chap. 2, pp. 21–60.
6. I. Epstein, J. A. Pojman, *An Introduction to Nonlinear Chemical Reactions* (Oxford Univ. Press, New York, 1998).
7. M. Isalan, C. Lemerle, L. Serrano, Engineering gene networks to emulate Drosophila embryonic pattern formation. *PLoS Biol.* **3**, e64 (2005).
8. E. Karzbrun, A. M. Tayar, V. Noireaux, R. H. Bar-Ziv, Programmable on-chip DNA compartments as artificial cells. *Science* **345**, 829–832 (2014).
9. M. Loose, E. Fischer-Friedrich, J. Ries, K. Kruse, P. Schwille, Spatial regulators for bacterial cell division self-organize into surface waves in vitro. *Science* **320**, 789–792 (2008).
10. D. Y. Zhang, G. Seelig, Dynamic DNA nanotechnology using strand-displacement reactions. *Nat. Chem.* **3**, 103–113 (2011).
11. S. M. Chirieleison, P. B. Allen, Z. B. Simpson, A. D. Ellington, X. Chen, Pattern transformation with DNA circuits. *Nat. Chem.* **5**, 1000–1005 (2013).
12. K. Montagne, R. Plasson, Y. Sakai, T. Fujii, Y. Rondelez, Programming an in vitro DNA oscillator using a molecular networking strategy. *Mol. Syst. Biol.* **7**, 476 (2011).
13. A. Padirac, T. Fujii, A. Estévez-Torres, Y. Rondelez, Spatial waves in synthetic biochemical networks. *J. Am. Chem. Soc.* **135**, 14586–14592 (2013).
14. M. C. Marchetti, J.-F. Joanny, S. Ramaswamy, T. B. Liverpool, J. Prost, M. Rao, R. A. Simha, Hydrodynamics of soft active matter. *Rev. Mod. Phys.* **85**, 1143–1189 (2013).
15. F. J. Nedelec, T. Surrey, A. C. Maggs, S. Leibler, Self-organization of microtubules and motors. *Nature* **389**, 305–308 (1997).
16. P. M. Bendix, G. H. Koenderink, D. Cuvelier, Z. Dogic, B. N. Koeleman, W. M. Brieher, C. M. Field, L. Mahadevan, D. A. Weitz, A quantitative analysis of contractility in active cytoskeletal protein networks. *Biophys. J.* **94**, 3126–3136 (2008).
17. T. Sanchez, D. T. Chen, S. J. DeCamp, M. Heymann, Z. Dogic, Spontaneous motion in hierarchically assembled active matter. *Nature* **491**, 431–434 (2012).
18. P. J. Foster, S. Fürthauer, M. J. Shelley, D. J. Needleman, Active contraction of microtubule networks. *eLife* **4**, e10837 (2015).
19. K.-T. Wu, J. B. Hishamunda, D. T. Chen, S. J. DeCamp, Y.-W. Chang, A. Fernández-Nieves, S. Fraden, Z. Dogic, Transition from turbulent to coherent flows in confined three-dimensional active fluids. *Science* **355**, eaal1979 (2017).
20. N. Kumar, R. Zhang, J. J. de Pablo, M. L. Gardel, Tunable structure and dynamics of active liquid crystals. *Sci. Adv.* **4**, eaat7779 (2018).
21. T. Torisawa, D. Taniguchi, S. Ishihara, K. Oiwa, Spontaneous formation of a globally connected contractile network in a microtubule-motor system. *Biophys. J.* **111**, 373–385 (2016).
22. Y. Ideses, V. Erukhimovitch, R. Brand, D. Jourdain, J. S. Hernandez, U. R. Gabinet, S. A. Safran, K. Kruse, A. Bernheim-Groswasser, Spontaneous buckling of contractile poroelastic actomyosin sheets. *Nat. Commun.* **9**, 2461 (2018).
23. J. Roostalu, J. Rickman, C. Thomas, F. Nédélec, T. Surrey, Determinants of polar versus nematic organization in networks of dynamic microtubules and mitotic motors. *Cell* **175**, 796–808.e14 (2018).
24. A. Senoussi, S. Kashida, R. Voituriez, J.-C. Galas, A. Maitra, A. Estevez-Torres, Tunable corrugated patterns in an active nematic sheet. *Proc. Natl. Acad. Sci.* **116**, 22464–22470 (2019).
25. R. Yoshida, T. Takahashi, T. Yamaguchi, H. Ichijo, Self-oscillating gel. *J. Am. Chem. Soc.* **118**, 5134–5135 (1996).
26. R. Yoshida, T. Ueki, Evolution of self-oscillating polymer gels as autonomous polymer systems. *NPG Asia Mater.* **6**, e107 (2014).
27. A. Cangialosi, C. Yoon, J. Liu, Q. Huang, J. Guo, T. D. Nguyen, D. H. Gracias, R. Schulman, DNA sequence–directed shape change of photopatterned hydrogels via high-degree swelling. *Science* **357**, 1126–1130 (2017).
28. A. J. Wollman, C. Sanchez-Cano, H. M. Carstairs, R. A. Cross, A. J. Turberfield, Transport and self-organization across different length scales powered by motor proteins and programmed by DNA. *Nat. Nanotechnol.* **9**, 44–47 (2014).
29. Y. Sato, Y. Hiratsuka, I. Kawamata, S. Murata, M. Ichiro, S.-I. Nomura, Micrometer-sized molecular robot changes its shape in response to signal molecules. *Sci. Robot.* **2**, eaal3735 (2017).
30. J. J. Keya, R. Suzuki, A. M. R. Kabir, D. Inoue, H. Asanuma, K. Sada, H. Hess, A. Kuzuya, A. Kakugo, DNA-assisted swarm control in a biomolecular motor system. *Nat. Commun.* **9**, 453 (2018).
31. O. J. N. Bertrand, D. K. Fygenson, O. A. Saleh, Active, motor-driven mechanics in a DNA gel. *Proc. Natl. Acad. Sci.* **109**, 17342–17347 (2012).
32. X. He, M. Aizenberg, O. Kuksenok, L. D. Zarzar, A. Shastri, A. C. Balazs, J. Aizenberg, Synthetic homeostatic materials with chemo-mechano-chemical self-regulation. *Nature* **487**, 214–218 (2012).
33. P. Gross, K. V. Kumar, S. W. Grill, How active mechanics and regulatory biochemistry combine to form patterns in development. *Annu. Rev. Biophys.* **46**, 337–356 (2017).
34. E. Hannezo, C.-P. Heisenberg, Mechanochemical feedback loops in development and disease. *Cell* **178**, 12–25 (2019).
35. K. Gavriljuk, B. Scocozza, F. Ghasemalizadeh, H. Seidel, A. P. Nandan, M. Campos-Medina, M. Schmick, A. Koseska, P. I. H. Bastiaens, A self-organized synthetic morphogenic liposome responds with shape changes to local light cues. *Nat. Commun.* **12**, 1548 (2021).
36. T. Fujii, Y. Rondelez, Predator–prey molecular ecosystems. *ACS Nano* **7**, 27–34 (2013).
37. K. Montagne, G. Gines, T. Fujii, Y. Rondelez, Boosting functionality of synthetic DNA circuits with tailored deactivation. *Nat. Commun.* **7**, 13474 (2016).
38. G. Urtel, M. Van Der Hofstadt, J.-C. Galas, A. Estevez-Torres, rEXPAR: An isothermal amplification scheme that is robust to autocatalytic parasites. *Biochemistry* **58**, 2675–2681 (2019).
39. M. Van Der Hofstadt, J.-C. Galas, A. Estevez-Torres, Spatiotemporal patterning of living cells with extracellular DNA programs. *ACS Nano* **15**, 1741–1752 (2021).
40. A. S. Zadorin, Y. Rondelez, J.-C. Galas, A. Estevez-Torres, Synthesis of programmable reaction-diffusion fronts using DNA catalyzers. *Phys. Rev. Lett.* **114**, 068301 (2015).
41. A. S. Zadorin, Y. Rondelez, G. Gines, V. Dilhas, G. Urtel, A. Zambrano, J.-C. Galas, A. Estevez-Torres, Synthesis and materialization of a reaction-diffusion French flag pattern. *Nat. Chem.* **9**, 990–996 (2017).
42. B. Martínez-Prat, J. Ignés-Mullol, J. Casademunt, F. Sagués, Selection mechanism at the onset of active turbulence. *Nat. Phys.* **15**, 362–366 (2019).
43. T. E. Bate, E. J. Jarvis, M. E. Varney, K.-T. Wu, Collective dynamics of microtubule-based 3D active fluids from single microtubules. *Soft Matter* **15**, 5006–5016 (2019).
44. S. Vedel, H. Bruus, Transient Taylor-Aris dispersion for time-dependent flows in straight channels. *J. Fluid Mech.* **691**, 95–122 (2012).

45. G. Gines, A. S. Zadorin, J.-C. Galas, T. Fujii, A. Estevez-Torres, Y. Rondelez, Microscopic agents programmed by DNA circuits. *Nat. Nanotechnol.* **12**, 351–359 (2017).
46. B. Lemma, N. P. Mitchell, R. Subramanian, D. J. Needleman, Z. Dogic, Active microphase separation in mixtures of microtubules and tip-accumulating molecular motors; arXiv:2107.12281 (2021).
47. H. W. H. van Roekel, L. H. H. Meijer, S. Masroor, Z. C. Félix Garza, A. Estévez-Torres, Y. Rondelez, A. Zagaris, M. A. Peletier, P. A. J. Hilbers, T. F. A. de Greef, Automated design of programmable enzyme-driven DNA circuits. *ACS Synth. Biol.* **4**, 735–745 (2015).
48. M. Dogterom, T. Surrey, Microtubule organization in vitro. *Curr. Opin. Cell Biol.* **25**, 23–29 (2013).
49. Y. Vyborna, J.-C. Galas, A. Estevez-Torres, DNA-controlled spatio-temporal patterning of a cytoskeletal active gel. *bioRxiv* 10.1101/2021.08.02.454703 , (2021).
50. A. Dupin, F. C. Simmel, Signalling and differentiation in emulsion-based multi-compartmentalized in vitro gene circuits. *Nat. Chem.* **11**, 32–39 (2019).
51. M. R. Jones, N. C. Seeman, C. A. Mirkin, Programmable materials and the nature of the DNA bond. *Science* **347**, 1260901 (2015).
52. Y. Zhao, F. Chen, Q. Li, L. Wang, C. Fan, Isothermal amplification of nucleic acids. *Chem. Rev.* **115**, 12491–12545 (2015).
53. K. Furuta, A. Furuta, Y. Y. Toyoshima, M. Amino, K. Oiwa, H. Kojima, Measuring collective transport by defined numbers of processive and nonprocessive kinesin motors. *Proc. Natl. Acad. Sci.* **110**, 501–506 (2013).
54. R. Subramanian, J. Gelles, Two distinct modes of processive kinesin movement in mixtures of ATP and AMP-PNP. *J. Gen. Physiol.* **130**, 445–455 (2007).
55. T. Wakamatsu, Y. Kitamura, Y. Kotera, N. Nakagawa, S. Kuramitsu, R. Masui, Structure of RecJ exonuclease defines its specificity for single-stranded DNA. *J. Biol. Chem.* **285**, 9762–9769 (2010).
56. J.-Y. Tinevez, N. Perry, J. Schindelin, G. M. Hoopes, G. D. Reynolds, E. Laplantine, S. Y. Bednarek, S. L. Shorte, K. W. Eliceiri, TrackMate: An open and extensible platform for single-particle tracking. *Methods* **115**, 80–90 (2017).
57. A. Baccouche, K. Montagne, A. Padirac, T. Fujii, Y. Rondelez, Dynamic DNA-toolbox reaction circuits: A walkthrough. *Methods* **67**, 234–249 (2014).
58. A. Senoussi, Design of molecular systems for artificial pattern formation and gene regulation. Ph.D. thesis, Sorbonne Université, 2020.
59. G. G. Borisy, J. M. Marcum, J. B. Olmsted, D. B. Murphy, K. A. Johnson, Purification of tubulin and associated high molecular weight proteins from porcine brain and characterization of microtubule assembly in vitro. *Ann. N. Y. Acad. Sci.* **253**, 107–132 (1975).
60. F.-A. Piedra, T. Kim, E. S. Garza, E. A. Geyer, A. Burns, X. Ye, L. M. Rice, GDP-to-GTP exchange on the microtubule end can contribute to the frequency of catastrophe. *Mol. Biol. Cell* **27**, 3515–3525 (2016).
61. M. Muraoka, H. Sakai, Effects of purinenucleotide analogues on microtubule assembly. *Cell Struct. Funct.* **24**, 305–312 (1999).
62. A. A. Hyman, S. Salser, D. N. Drechsel, N. Unwin, T. J. Mitchison, Role of GTP hydrolysis in microtubule dynamics: Information from a slowly hydrolyzable analogue, GMPCPP. *Mol. Biol. Cell* **3**, 1155–1167 (1992).
63. T. Nakata, S. Niwa, Y. Okada, F. Perez, N. Hirokawa, Preferential binding of a kinesin-1 motor to GTP-tubulin–rich microtubules underlies polarized vesicle transport. *J. Cell Biol.* **194**, 245–255 (2011).

Acknowledgments: We thank H. Berthoumieux, V. Bormuth, M. Elez, A. Genot, G. Gines, N. Lobato-Dauzier, A. Maitra, Y. Vyborna, L. Robert, Y. Rondelez, and R. Voituriez for insightful discussions and K. Furuta and Z. Gueroui for their gift of kinesin plasmids. **Funding:** This work has been funded by the European Research Council (ERC) under the European's Union Horizon 2020 programme (grant No 770940, A.E.-T.), by the Ville de Paris Emergences program (Morphoart, A.E.-T.), and by MITI CNRS (J.-C. G.). **Author contributions:** A.S. performed research, and all authors designed research, analyzed the data, and wrote the manuscript. **Competing interests:** The authors declare that they have no competing interests. **Data and materials availability:** All data needed to evaluate the conclusions in the paper are present in the paper and/or the Supplementary Materials.

Submitted 13 April 2021
Accepted 2 November 2021
Published 17 December 2021
10.1126/sciadv.abi9865

ScienceAdvances

Programmed mechano-chemical coupling in reaction-diffusion active matter

Anis SenoussiJean-Christophe GalasAndré Estevez-Torres

Sci. Adv., 7 (51), eabi9865. • DOI: 10.1126/sciadv.abi9865

Science Advances (ISSN) is published by the American Association for the Advancement of Science. 1200 New York Avenue NW, Washington, DC 20005. The title *Science Advances* is a registered trademark of AAAS.